EcoMat

WILEY

EcoMat
FUNCTIONAL MATERIALS FOR GREEN ENERGY AND ENVIRONMENT

RESEARCH ARTICLE OPEN ACCESS

Current-Dependent Coupling Behaviors Inspired Wide-Current Cyclable Zn Metal Anode

Yanpeng Guo[1] | Lutong Shan[2] | Yongqiang Yang[1] | Junhua Zhou[1] | Zijian Zheng[1,3,4]

[1]Department of Applied Biology and Chemical Technology, Faculty of Science, The Hong Kong Polytechnic University, Hung Hom, Hong Kong SAR | [2]Department of Chemistry, University of Manchester, Manchester, UK | [3]Research Institute for Intelligent Wearable Systems (RI-IWEAR), The Hong Kong Polytechnic University, Hung Hom, Hong Kong SAR | [4]Research Institute for Smart Energy (RISE), The Hong Kong Polytechnic University, Hung Hom, Hong Kong SAR

Correspondence: Zijian Zheng (tczzheng@polyu.edu.hk)

Received: 14 March 2025 | **Revised:** 2 April 2025 | **Accepted:** 3 April 2025

Funding: This work was supported by the RGC Postdoctoral Fellowship Scheme (PDFS2223_5S01), the RGC Research Impact Fund (R5019-22), the Innovation and Technology Fund (GHP/047/20GD and PRP/055/21FX).

Keywords: calendar | corrosion | current density | cycling | zinc metal anode

ABSTRACT

Aqueous zinc metal batteries (AZMBs) provide a safe and cost-effective solution to meet the future demand for large-scale energy storage applications. Stable cycling of the Zn metal anode (ZMA) within a wide current range from 0.2 to 10 mA cm^{-2} is considered one of the most critical requirements to enable AZMBs. However, current studies show that ZMAs may cycle at either high- or low-current densities, but it is difficult to simultaneously achieve stable cycling at this wide current range. Herein, we study the current-dependent coupling interactions among plating, stripping, and corrosion of ZMAs. We reveal that low-current plating/stripping of Zn leads to unfavorable morphological and crystallographic evolution, which results in serious surface corrosion and rapid failure. In contrast, high-current plating/stripping of Zn can enrich its highly stable (002) facets and form localized high-concentration electrolyte layers with solvated aggregates, which consequently suppresses hydrogen evolution reaction, dendrite formation, and surface corrosion. By understanding these current-dependent coupling behaviors, we develop a high-current-engineered Zn anode that enables long-term cycling across a wide current range, including a record-breaking cycling of 4500 h at 0.2 mA cm^{-2}. This work offers new fundamental insights and a feasible engineering strategy to significantly boost the stability of ZMAs.

1 | Introduction

Battery technology is a crucial enabler of the global energy transition from conventional fossil fuel to green and sustainable energy resources to achieve worldwide decarbonization [1–4]. In comparison to the prevalent lithium-ion batteries, aqueous zinc metal batteries (AZMBs) demonstrate unparalleled safety performance, environmental benignity, cost-effectiveness, and earth abundance. Together with its moderate energy density, AZMBs attract progressive attention for large-scale stationary energy-storage applications [5–7]. High-performance Zn metal anode (ZMA) is one of the primary cornerstones that enable the practical deployment of AZMBs [8–10]. The intrinsic plating/stripping behaviors of ZMAs and corrosion-prone aqueous electrolyte systems are commonly believed to readily trigger severe dendrite nucleation and hydrogen evolution reactions (HERs) upon plating at high currents, leading to rapid cell failure [11–13].

Yanpeng Guo and Lutong Shan contributed equally to this study.

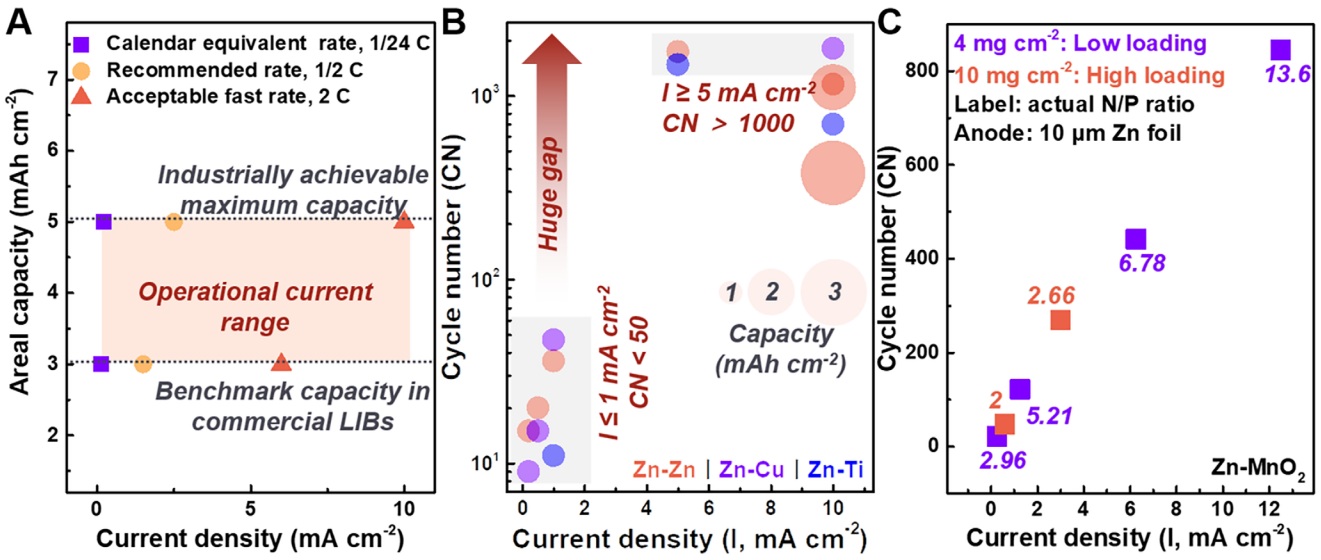

FIGURE 1 | Rapid Zn anode failure upon low-current cycling. (A) Acceptable operating current range of the anode based on the cathode capacities and rate requirements for practical grid-scale energy storage applications. (B) Cyclability of Zn anodes using various cell configurations. (C) Cyclability of Zn-MnO_2 full cells at different cycling currents and N/P ratios.

Current researches on ZMAs largely focus on addressing the deposition-induced dendrite and HER issue to promote their high-current cycling stability via solvation structure design [14–16], artificial interface engineering [17–20], plating texture regulation [21–23], and so on. However, unlike prevailing lithium batteries using Li-containing cathodes and requiring initial lithium plating, the predominant cathodes for AZMBs are manganese-based or vanadium-based oxide materials through a typical intercalation/extraction mechanism. The first step of these Zn-free cathodes upon cycling is to discharge, which corresponds to the stripping reactions on the ZMAs [24–27]. The initial stripping process through a solid–liquid conversion can lead to exposure of fresh highly reactive Zn surface, serious surface damage, and unavoidable crystallographic evolution. So far, insufficient attention has been paid to the stripping mechanisms of ZMAs, as well as their impact on cycling and calendar stability.

Additionally, from the viewpoint of practical application, an energy-storage AZMB should be capable of continuously charging or discharging for more than 2 h under normal operational conditions, equivalent to a C rate of less than 1/2 C [1]. In instances where the battery is to regulate power frequency or to mitigate the fluctuations of renewable energy, a charging/discharging rate of 2 C is deemed needed. Of parallel importance, a battery should ensure a long calendar life exceeding 10 years, which is equivalent to more than 3000 cycles at a low rate of 1/24 C [3]. However, there is a knowledge gap regarding the coupling behaviors among Zn plating, stripping, and corrosion across such a wide current range from 1/24 C to 2 C. There is also a lack of strategies to improve ZMA cyclability over this wide range of currents.

In this study, we explore the current-dependent plating, stripping, and corrosion mechanisms of ZMAs and their interrelated electrochemical behaviors. We analyze morphological changes, crystallographic features, hydrogen evolution kinetics, corrosion mechanisms, and electrolyte solvation structure across various currents. Our results show that Zn stripping causes more severe corrosion and gas production than plating, with increased (002) facet exposure at higher stripping currents reducing corrosion. Corrosion is even worse during resting due to altered ion concentration distribution. As the stripping current increases, the solvation structure shifts from contact-ion-pair dominance to solvated aggregates. High-current cells experience less corrosion due to favorable interelectrode potential distributions. High-current plating also enables dendrite-free, HER-resistant deposition of dense Zn microblocks, unlike low-current plating, which forms easily corroded mossy deposits. Understanding these behaviors further leads to the development of a high-current-engineered ZMA (HC-Zn) that supports stable cycling from 0.2 to 10 mA cm^{-2}, with a lifespan exceeding 4500 h at 0.2 mA cm^{-2}. Zn-MnO_2 full cells with HC-Zn sustain over 500 cycles at low current. This work provides fundamental guidance for developing better ZMAs and offers new insights for advancing wide-current cyclable AZMBs.

2 | Results and Discussion

2.1 | Rapid Zn Anode Failure Upon Low-Current Cycling

Large-scale stationary energy storage applications require stable cycling of ZMAs across a wide current range from at least 1/24 C to 2 C. Taking into account that the areal capacity of a commercial battery's electrode is normally in the range of 3–5 mAh cm^{-2}, the charge/discharge current density range can then be calculated as 0.12–10 mA cm^{-2} (Figure 1A). In this range, our preliminary cycling tests revealed that symmetric Zn-Zn cells sustained smooth cycling for over 1000 cycles at high-current densities (5 and 10 mA cm^{-2}) (Figures 1B and S1). In contrast, significant voltage fluctuations and cell shorts were already observed within 40 cycles when low-current densities (0.2, 0.5, and 1 mA cm^{-2}) were employed. When the capacity increased to 3 mAh cm^{-2}, the cell still maintained

a good stability to 400 cycles at 10 mA cm^{-2}, while it could hardly operate at 0.2 mA cm^{-2}. Similarly, the Zn-Cu half-cell exhibited a high average coulombic efficiency (CE) of over 99% within 1800 cycles when cycling at 10 mA cm^{-2}. As the current decreased to 0.2 mA cm^{-2}, a pronounced short circuit was observed during the ninth plating, which led to CEs less than 10% in the following cycles (Figure S2). An analogous current-dependent behavior, whereby a higher current contributes to enhanced cycling reversibility, was also demonstrated using Zn-Ti half cells (Figure S3).

Lower cycling current density also resulted in more severe capacity decay in Zn-MnO_2 full cells. As is known, the intrinsic dissolution issue of the MnO_2 cathode can adversely affect the performance. To amplify the impact of Zn on cyclability, ultrathin Zn foil with a thickness of 10 μm was specially adopted for full-cell tests (Figure 1C). For the low-loading cell, when the current density was decreased from 6.25 to 0.25 mA cm^{-2}, the capacity decay per cycle increased by 24-fold, from 0.25 to 6 mAh g^{-1} cycle^{-1} (Figure S4). For the high-loading cell, the capacity decay was increased sixfold as the current density decreased from 3 to 0.6 mA cm^{-2}. For cells with a similar N/P ratio, a high current of 3 mA cm^{-2} can elongate a 10-fold lifespan compared to a low current of 0.25 mA cm^{-2}. Moreover, cells with a low N/P ratio (2.66) and high current (3 mA cm^{-2}) outperform those with a high N/P ratio (5.21) and low current (1.25 mA cm^{-2}). In this sense, it is highly imperative to systematically evaluate the current-dependent electrochemical behaviors of ZMAs and concentrate more on advancing their wide-current cyclability for the industrial deployment of AZMBs.

2.2 | Current-Dependent Plating Behaviors and Corrosion Resistant Properties

Zn exhibits a markedly higher density (7.14 g cm^{-3}) compared to alkaline metals Zn exhibits a markedly higher density (7.14 g cm^{-3}) compared to alkaline metals (Li: 0.53 g cm^{-3}; Na: 0.97 g cm^{-3}; and K: 0.86 g cm^{-3}), indicating significantly reduced volume and thickness fluctuations upon plating/stripping. At the same plating capacity, a thinner thickness change could potentially elongate the morphological tailoring effect of the substrate on Zn deposits [27]. The aqueous electrolyte also bestows swift mass transport kinetics, preventing the rapid ion depletion and space-charge layer formation that trigger dendrite nucleation upon high-current plating. As a result, Zn exhibited an intrinsically high critical current density (CCD) of up to 60 mA cm^{-2} at a capacity of 3 mAh cm^{-2} (Figure 2A). Continuous plating under various currents was also performed (Figure 2B). As the current density increased from 1 to 50 mA cm^{-2}, the critical capacity for short-circuiting rose sharply from 11.2 to 42.6 mAh cm^{-2}. Even at extremely high-current densities of 100 and 200 mA cm^{-2}, the critical capacities surpassed that at 1 mA cm^{-2}. Zn deposits formed at high-current densities (50, 100, and 200 mA cm^{-2}) and their corresponding maximum workable capacities (42, 20, and 15 mAh cm^{-2}) were highly uniform and dense (Figure 2C–E). In contrast, Zn deposits at 1 mA cm^{-2} and 11 mAh cm^{-2} were porous clusters composed of thin filaments (Figure 2F). These findings suggested a low propensity for dendrite growth in AZMBs, particularly in energy-storage applications.

Subsequently, we examined the nucleation and growth behavior of Zn during plating at different current densities. At a high-current density of 10 mA cm^{-2}, the nucleation overpotential was 168.3 mV (Figure S5), resulting in high nuclei density and small nuclei size at 0.2 mAh cm^{-2} (Figure 2G). As the capacity increased to 1 mAh cm^{-2}, Zn nuclei developed into uniform microblocks with homogeneous distribution. At a capacity of 3 mAh cm^{-2}, the Zn deposits became interconnected, forming a smooth layer. Corresponding laser microscopy images of Zn deposits at 10 mA cm^{-2} revealed a smooth top surface with minimal height fluctuations, indicating uniform growth behavior at high-current densities. Conversely, at a low-current density of 0.5 mA cm^{-2}, the nucleation overpotential significantly decreased to 66.4 mV, leading to localized deposition with low nuclei density under a capacity of 0.2 mAh cm^{-2} (Figure 2H). As the current increased to 1 mAh cm^{-2}, Zn clusters with thin filaments began to form. At a capacity of 3 mAh cm^{-2}, the mossy Zn clusters expanded, and substantial amounts of by-product $ZnSO_4{\cdot}3Zn(OH)_2{\cdot}5H_2O$ (denoted as ZSH, PDF#78-0246) flakes also formed near the clusters. Laser microscopy images of Zn deposits at 0.5 mA cm^{-2} showed increasing height fluctuations from 31.7 to 88.5 μm and 264 μm as the plating capacity increased, demonstrating nonuniform growth behavior. Accordingly, the HER overpotential of Zn deposits at 0.5 mA cm^{-2} decreased by ~160 mV compared to that at 10 mA cm^{-2} (Figure 2I). The Tafel plot of the Zn deposits at 0.5 mA cm^{-2} was also 11.2 mV lower than that at 10 mA cm^{-2} (Figure 2J). The intensified hydrogen evolution and corrosion tendency at low-current densities likely contributed to the increased formation of ZSH during the Zn plating process, as indicated by the X-ray diffraction (XRD) patterns (Figure 2K). These results suggested that the stability of ZMA decreased with reduced current density during plating.

2.3 | Current-Dependent Stripping Behaviors and Exposed Facet Orientations

We also observed significant differences in surface morphologies and facet orientations of Zn after stripping. At a low-current density of 0.5 mA cm^{-2}, localized Zn dissolution was evident at a capacity of 0.2 mAh cm^{-2} (Figure 3A). Concurrently, nanosheets began to form on the newly exposed Zn surface. As the stripping capacity increased to 1 mAh cm^{-2}, randomly distributed pits covered by thin flakes emerged. At a capacity of 3 mAh cm^{-2}, these flakes became even thicker and more prevalent in the vicinity of stripping sites rather than in non-stripping areas. Elemental mapping and energy dispersive spectrometry (EDS) in Figure 3B revealed that the flakes contained high levels of Zn, O, and S with an atomic ratio of 37.2:59.6:3.2, indicating the presence of in situ generated ZSH by-products. This suggested that severe corrosion of freshly exposed Zn metal occurs at low-current densities. In contrast, after being stripped at a high-current density of 10 mA cm^{-2}, the Zn surface exhibited more uniformly distributed dissolution spots at 0.2 mAh cm^{-2}. Enlarged SEM images of stripped Zn revealed textured cracks (Figure 3C). As the capacity increased to 1 mAh cm^{-2}, the dissolution pits grew larger. At a capacity of 3 mAh cm^{-2}, the Zn surface maintained a morphology characterized by vertical cracks. Corresponding elemental mapping and EDS in Figure 3D showed no S signal, indicating suppressed corrosion of the exposed surface.

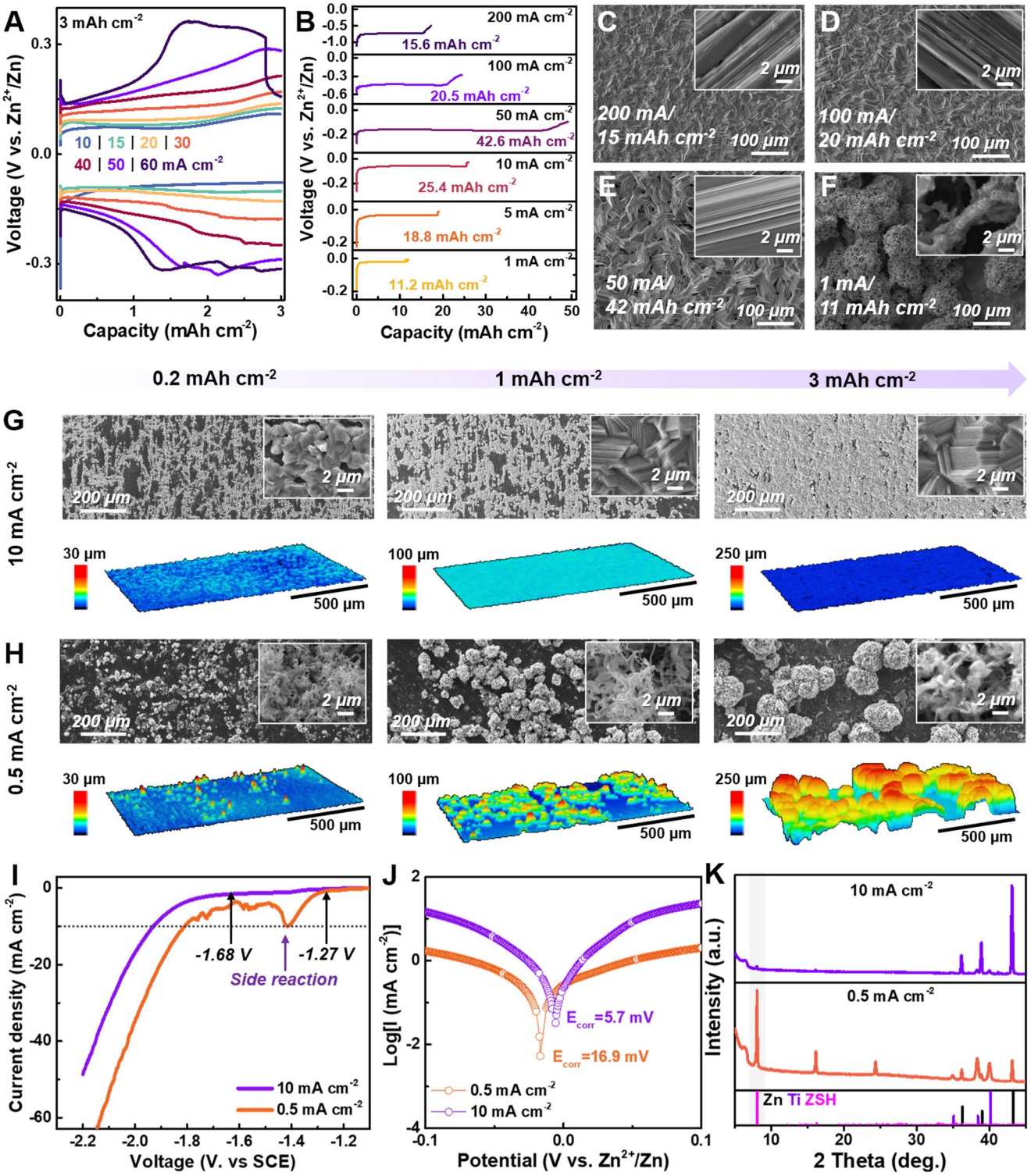

FIGURE 2 | Current-dependent plating behaviors and corrosion-resistant properties (A) Critical current density of the Zn anode under a capacity of 3 mAh cm^{-2}. (B) Voltage–time profiles upon continuous plating at various current densities, where the abrupt voltage drop indicated the battery was short by dendritic or mossy Zn growth. (C–F) Morphologies of Zn deposits under various current densities and corresponding maximum allowable capacities. (G, H) Scanning electron microscope (SEM) and laser microscope images of Zn deposits at 10 mA cm^{-2} (G) and 0.5 mA cm^{-2} (H) with various plating capacities. (I–K) Hydrogen evolution reaction curves (I), Tafel plots (J), and X-ray diffraction patterns (K) of Zn deposits at various current densities. Capacity: 3 mAh cm^{-2}.

The textured morphologies observed during high-current stripping suggested potential preferential orientations. Transmission electron microscope (TEM) images of the Zn electrode after stripping at 10 mA cm^{-2} and 5 mAh cm^{-2} showed large crystalline regions with a lattice spacing of 0.23 nm and intersection angles of 60°, indicating preferential exposure of (002) facets (Figure 3E). In contrast, the stripped Zn at 0.5 mA cm^{-2} and 5 mAh cm^{-2} exhibited crystalline domains with a lattice spacing of 0.24 nm or

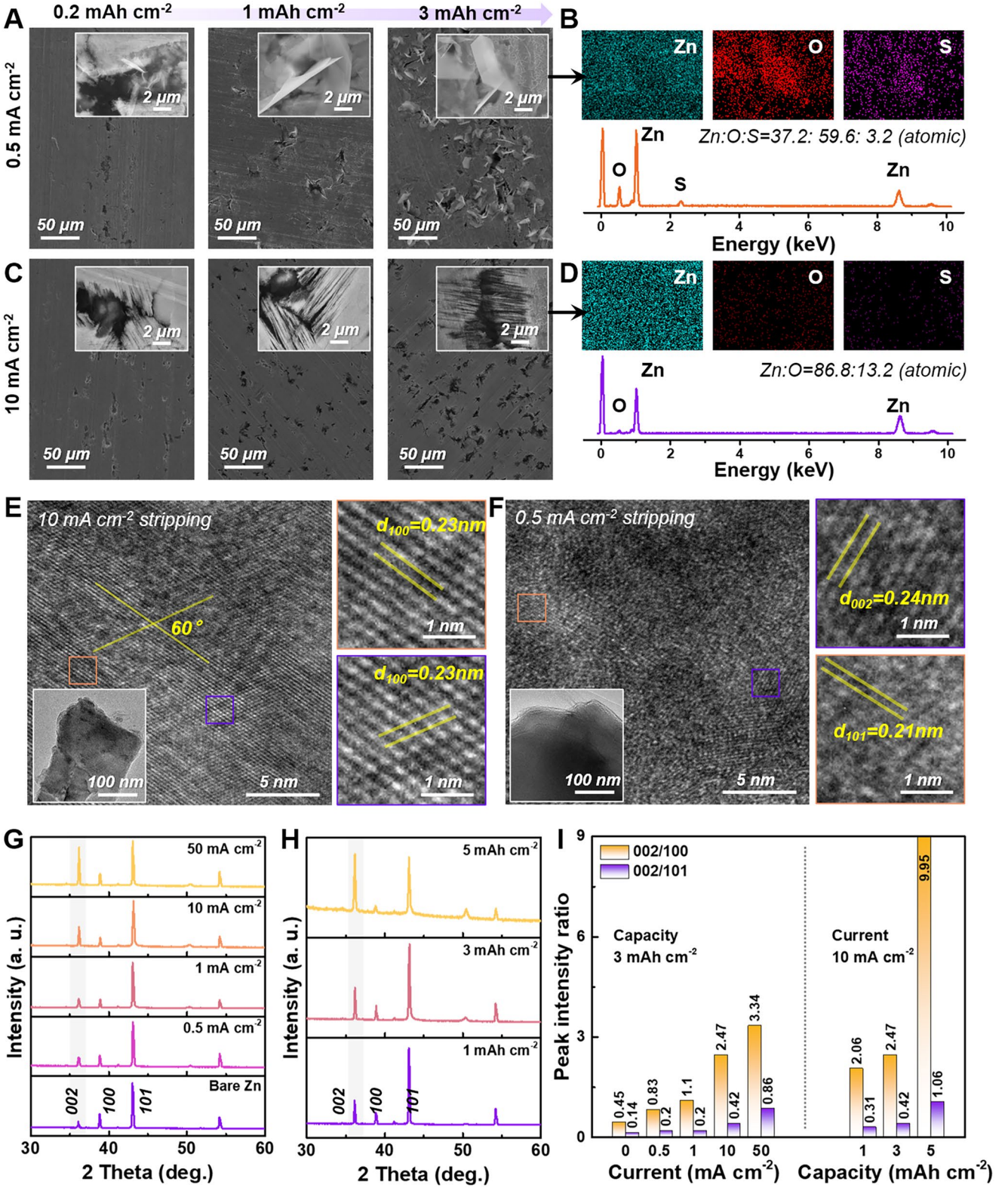

FIGURE 3 | Current-dependent stripping behaviors and exposed facet orientations. (A, B) Morphology of Zn electrode after stripping at 0.5 mA cm^{-2} for various capacities (A) and corresponding elemental mapping and energy dispersive spectrometry (B), showing the formation of ZSH by-products at the vicinity of fresh stripped Zn surface. (C, D) Morphology of Zn electrode after stripping at 10 mA cm^{-2} for various capacities (C) and corresponding elemental mapping and energy dispersive spectrometry (D), showing a highly textured stripping morphology without by-product formation. (E, F) Transmission electron microscope (TEM) images of the Zn electrode after stripping at 10 mA cm^{-2} (E) and 0.5 mA cm^{-2} (F) with a fixed capacity of 5 mAh cm^{-2}. (G) X-ray diffraction patterns of Zn electrode after stripping at various current densities (Capacity: 3 mAh cm^{-2}). (H) X-ray diffraction patterns of Zn electrode stripping at 10 mA cm^{-2} for various capacities. (I) Peak intensity ratios of (002)/(100) and (002)/(101) facets under different stripping conditions.

0.21 nm, corresponding to the exposure of (100) facets or other potential facets (Figure 3F). Figure 3G presented the XRD patterns of Zn electrodes after stripping at 0.5, 1, 10, and 50 mA cm^{-2} under a fixed capacity of 3 mAh cm^{-2}. The bare Zn electrode exhibited a (101) and (100) dominated XRD pattern. Notably, the peak intensity of (002) facet increased with the current density. Furthermore, at a fixed high-current density of 10 mA cm^{-2}, the peak intensity of (002) facet also increased as the stripping capacity rose from 1 to 5 mAh cm^{-2} (Figure 3H). As the current density increased from 0.5 to 10 mA cm^{-2}, the peak intensity ratios of (002)/(100) and (002)/(101) increased threefold and twofold respectively (Figure 3I). At a stripping capacity of 5 mAh cm^{-2}, the peak intensity ratios of (002)/(100) and (002)/(101) reached 9.95 and 1.06, respectively, representing an improvement of 22-fold and 7.5-fold compared to the bare Zn. These findings confirmed the intensified (002) facet exposure upon high-current stripping, particularly at greater depths of dissolution.

To elucidate the underlying mechanism of the preferential stripping of the (002) facet at high-current densities, a tri-electrode system with a saturated calomel electrode (SCE) as the reference was employed to monitor the voltage profiles of the stripping electrode (SE) at various current densities (Figure 4A). The peak stripping potential and stripping overpotential at 10 mA cm^{-2} were higher than those at 0.5 mA cm^{-2}, indicating a greater driving force for Zn dissolution into the electrolyte (Figure 4B). Zn has a hexagonally close-packed (hcp) crystalline structure, where the (002) facet is the most closely packed with minimal dangling bonds, the strongest Zn-Zn atomic bonding, and optimal thermodynamic stability [23, 28, 29]. Density functional theory (DFT) calculations (Figure 4C) revealed that the extraction energy of a Zn atom from the (002) facets was 1.88 eV, higher than from the (101) facet (1.57 eV) and the (100) facet (1.62 eV). Corresponding charge density difference maps of the three facets further confirmed the stronger electron cloud combination within the (002) crystal planes (Figure S6). The increased stripping potential at high-current densities facilitates the dissolution of Zn atoms from the (002) facets, thereby exposing more (002) facets. The (002) facet was calculated to exhibit the highest energy barrier of 1.32 eV for the HER, compared to the (100) facet (0.85 eV) and (101) facet (0.55 eV), conferring superior anti-corrosion and anti-HER capabilities.

Figure 4E compares the stripping behaviors under high-current and low-current conditions. During low-current plating, the bare Zn anode, dominated by (101)/(100) facets, preferred to dissolve along these facets due to their low Zn extraction energy barriers and low stripping driving force. The exposure of fresh (101) and (100) facets upon stripping led to severe chemical corrosion, hydrogen evolution, and by-product formation. In contrast, the increased stripping driving force at high-current densities favors dissolution along the (002) facets. This tendency promotes the perpendicular dissolution of (100) facets to expose more (002) facets, resulting in the vertical cracks observed in SEM characterizations. The enriched exposure of (002) facets after high-current stripping enhances resistance to hydrogen evolution, self-dissolution, and (electro)chemical corrosion.

In situ optical imaging with an in-plane microdevice was used to visualize the Zn plating/stripping processes. At a low-current density (Figure 4F), Zn deposition on the plating electrode (PE) resulted in non-uniform nucleation and growth, while Zn dissolution on the SE was locally intensified with substantial gas bubble formation. During the subsequent re-plating, the gas bubbles enlarged, indicating severe chemical corrosion between the freshly exposed Zn surface and the electrolyte. In contrast, at a tenfold increase in current density (Figure 4G), both Zn deposition on PE and dissolution on SE were highly uniform, with no gas bubbles observed on either electrode, indicating inhibited (electro)chemical corrosion at high-current densities. Additionally, when the plating time of the high-current cell device was extended to 0.2 and 0.5 h, few gas bubbles were observed (Figure 4H). However, when the high-current cell device was aged in the electrolyte for 0.9 h after plating for 0.1 h, slight bubbles from corrosion became visible at the stripped Zn electrode (Figure 4I). This suggested that corrosion on the high-current stripped Zn was more severe at rest than during high-current stripping [30, 31]. Simulations using COMSOL Multiphysics indicated that high-current stripping created a local environment of a highly concentrated electrolyte, showing an elevated concentration (Figure S7). Compared to the bare electrolyte at rest or low-current stripping (Figure 4J), the transient high-concentration electrolyte layer formed during high-current stripping resulted in a solvation structure of aggregates (AGGs), which can lessen the decomposition of water molecules, ultimately protecting the freshly stripped Zn surface from (electro)chemical corrosion.

These experiments reflected that gas evolution primarily results from chemical corrosion between the newly exposed Zn surface and the electrolyte during Zn dissolution, rather than from the electrochemical reduction of the electrolyte during Zn deposition. The depth of chemical corrosion during Zn dissolution was associated with the aging duration, stripping capacity, and current-dependent morphology and facet orientations. Thus, increasing the capacity during low-current cycling or introducing additional aging can significantly impair the cycling stability of Zn anodes (Figure S8).

2.4 | Current-Dependent Corrosion Behaviors

The potential difference between Zn deposits and the underlying substrate at one electrode could lead to galvanic corrosion [32, 33]. If the Zn deposits have a higher potential than the substrate, electrolyte decomposition and Zn self-dissolution may occur on the deposits and substrate, respectively. Conversely, if the substrate has a higher potential, the opposite behavior occurs (Figure 5A). Figure 5B illustrates the profiles of galvanic currents generated by Zn electrodes after plating or stripping. The galvanic current was only 11.72 μA for Zn deposited at a high-current density of 10 mA cm^{-2}, indicating significantly reduced corrosion compared to the high galvanic current of 34.07 μA of Zn deposited at 1 mA cm^{-2}. A similar trend was observed after stripping: the galvanic current was 19.72 μA after stripping at 10 mA cm^{-2}, much lower than the 41.17 μA observed after stripping at 1 mA cm^{-2}.

In addition to chemical corrosion, electrochemical corrosion via external circuit leakage during testing was another key factor affecting the cyclability of ZMAs (Figure 5C) [34, 35]. Electrolyte decomposition occurs on the electrode with the higher potential, while metal dissolution occurs on the electrode with the lower potential. A tri-electrode configuration was used for real-time monitoring of the voltage evolutions of two electrodes. At a low-current

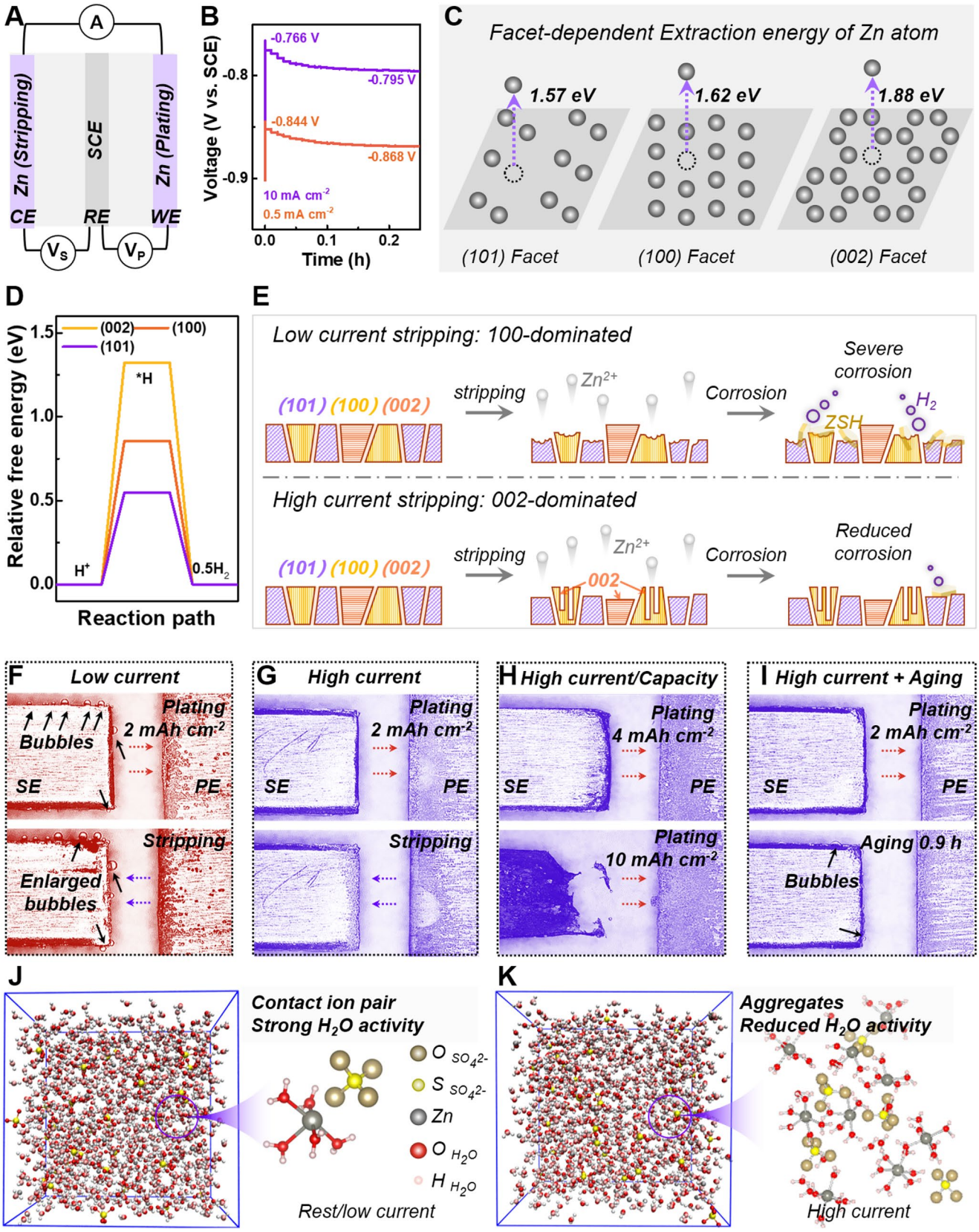

FIGURE 4 | Legend on next page.

density of 0.2 mA cm^{-2}, both stripping and plating processes exhibited overpotentials. During subsequent stripping, the plating locations on the SE varied, resulting in non-uniformity, as indicated by the two overpotential spikes in the voltage profile (Figure 5D). When the current was increased to 10 mA cm^{-2}, the plating on the SE was constant and homogenous, as indicated by the absence of additional potential spikes (Figure 5E). Figure 5F summarizes the voltage gaps between the PE and SE (Figure S9). As previously

FIGURE 4 | Zn plating. Mechanistic interpretations of the anti-corrosion capability during high-current stripping. (A) Setup of the tri-electrode system to monitor the voltage profiles during stripping. (B) Voltage–time profiles upon stripping at 10 and 0.5 mA cm^{-2}. (C, D) Facet-dependent extraction energy of Zn atom (C) and relative free energy of the hydrogen evolution reaction (D) using density functional theory calculations. (E) Schematic illustrations of the stripping and corrosion behaviors under both high-current and low-current conditions. (F–I) In situ optical images of the symmetrical cell device upon plating at 2 mA cm^{-2} for 1 h (2 mAh cm^{-2}) (F), plating at 20 mA cm^{-2} for 0.1 h (2 mAh cm^{-2}) (G), plating at 20 mA cm^{-2} for 0.2 h (4 mAh cm^{-2}) and 0.5 h (10 mAh cm^{-2}) (H), plating at 20 mA cm^{-2} for 0.1 h (2 mAh cm^{-2}) followed by resting for additional 0.9 h (I). (J, K) solvation structures at the Zn–electrolyte interface at rest/low-current stripping (J) or high-current stripping (K).

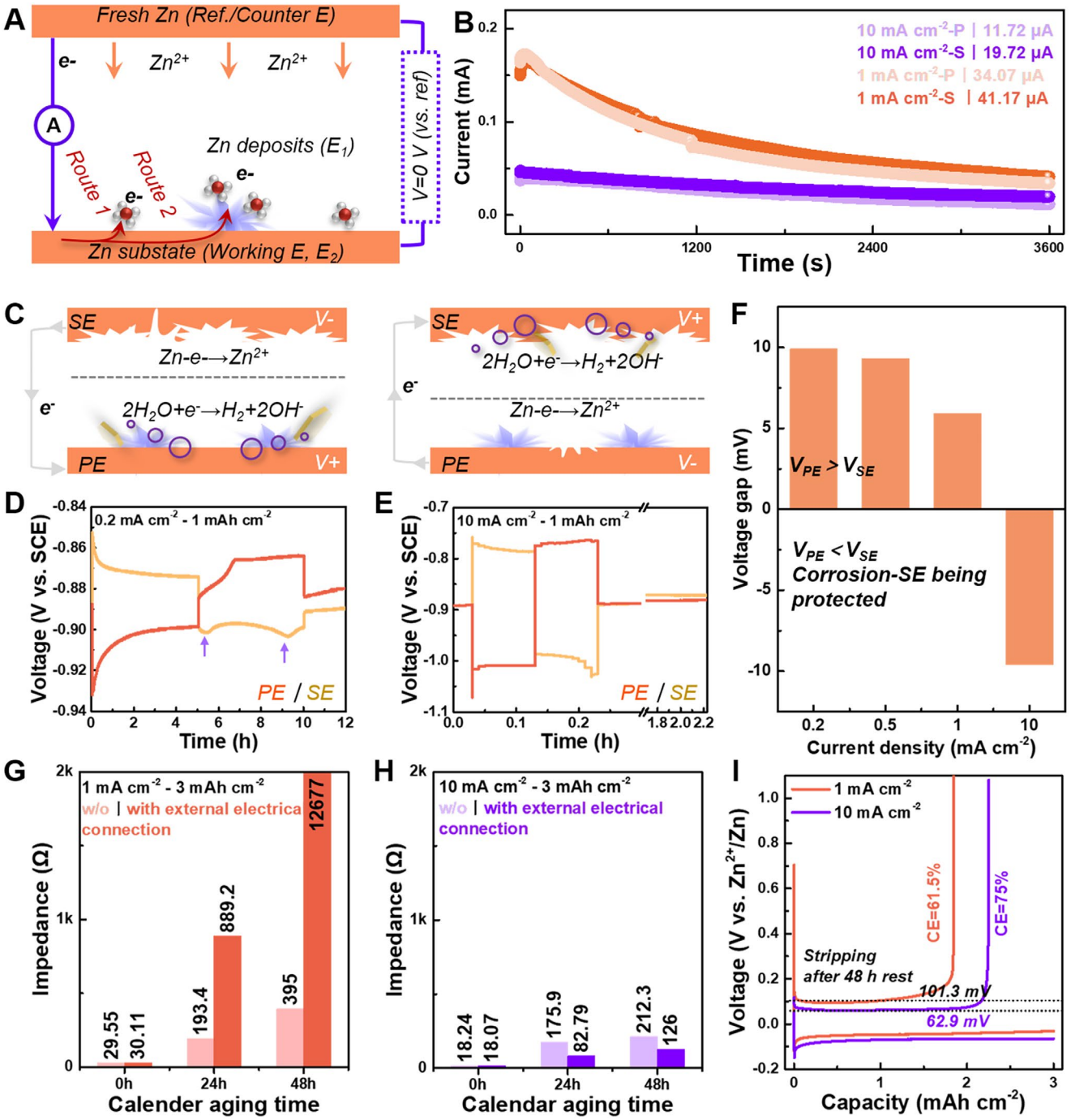

FIGURE 5 | Current-dependent corrosion behaviors. (A) Schematic illustration of the galvanic corrosion on individual electrodes. (B) Galvanic corrosion curves of the Zn foils after plating and stripping at currents of 10 or 1 mA cm^{-2}. (C) Schematic illustration of the electrochemical corrosion between two electrodes through external electrical connection and electron flow. (D, E) Voltage profiles of the stripping electrode (SE) and plating electrode (PE) at 0.2 mA cm^{-2} (D) and 10 mA cm^{-2} (E) using tri-electrode setup. (F) Voltage gaps between two electrodes during plating/stripping at various current densities. (G, H) Time-dependent impedances of symmetric Zn-Zn cells after plating at 1 mA cm^{-2} (G) and 10 mA cm^{-2} (H). Capacity: 3 mAh cm^{-2}. (I) Plating/stripping profiles of Zn-Ti half cells after 48 h resting with Zn deposits obtained at 1 or 10 mA cm^{-2}.

discussed, the SE was more susceptible to reacting with the electrolyte and corrosion. Compared to the low-current condition, the high-current PE exhibited a lower potential, thereby protecting the SE against severe corrosion.

The time-dependent impedance evolutions of symmetric Zn-Zn cells upon rest were measured to reflect the depth of corrosion (Figure S10). The cells were rested with or without connection to the external battery testing systems to ascertain the impact of electrochemical corrosion and the flow of leakage current between the two electrodes. For cells (capacity 3 mAh cm^{-2}) after plating at 1 mA cm^{-2}, the initial charge-transfer impedance ($\boldsymbol{R}_{ct}$) was approximately 30 Ω, which increased to 193.4 Ω (24 h) and 395 Ω (48 h), respectively (Figure 5G). The external electrical connection contributed to an additional impedance increase by 695.8 Ω due to coupled electrochemical corrosion between the two electrodes. The $\boldsymbol{R}_{ct}$ reached an unparalleled value of over 10 000 Ω after 48 h aging, indicating complete charge-transfer failure. For cells plating at 10 mA cm^{-2}, reduced impedance rises were observed with $\boldsymbol{R}_{ct}$ values of approximately 18 Ω (fresh), 175.9 Ω (24 h) and 212.3 Ω (48 h) (Figure 5H). In contrast to the 1 mA cm^{-2} condition, the additional connection and electron flow between the high-current (10 mA cm^{-2}) plated and stripped Zn electrodes resulted in a notable impedance decrease by 93.1 Ω (24 h) and 86.3 Ω (48 h). Comparable results were obtained when Zn-Ti half cells were employed (Figure S11). Plating at 10 mA cm^{-2} also led to an improved reversible capacity of 2.25 mAh cm^{-2} (1.85 mAh cm^{-2} at 1 mA cm^{-2}) and a lower stripping voltage hysteresis of 62.9 mV (101.3 mV at 1 mA cm^{-2}) after 48 h resting, indicating suppressed corrosion within high-current cells (Figure 5I).

2.5 | Current-Dependent Coupling Electrochemical Behaviors of Zn

The aforementioned comprehensive studies revealed that Zn stripping causes more severe corrosion and gas production than plating. Such stripping-induced corrosion is even worse during resting due to altered ion concentration distribution. In addition, different from prevailing lithium metal anodes, low-current plating of ZMAs led to the formation of unevenly distributed, mossy Zn clusters on the PE. This morphological characteristic resulted in poor substrate affinity and low electrode coverage, triggering strong galvanic corrosion (Figure 6A). Additionally, these mossy clusters have a higher tendency toward HER, facilitating the formation of insulating by-products and gas evolution. This led to a heterogeneous distribution of ions and electrons at the electrolyte–Zn interface, causing non-uniform deposition and dissolution. Concurrently, the formation of localized pits and the exposure of highly active fresh Zn surfaces on the SE exacerbated adverse chemical corrosion, particularly during high-capacity long-term stripping, resulting in more gas bubbles and by-products. The external electrical leakage during cycling on the testing device further intensified the electrochemical corrosion of the SE. Consequently, ZMAs exhibited markedly inferior cyclability at low-current densities.

In contrast, the high-current plating of ZMAs actually resulted in a more homogenous and dense morphology with suppressed HER activity and high substrate coverage, thereby inhibiting the gas evolution and galvanic corrosion on the PE (Figure 6A). The

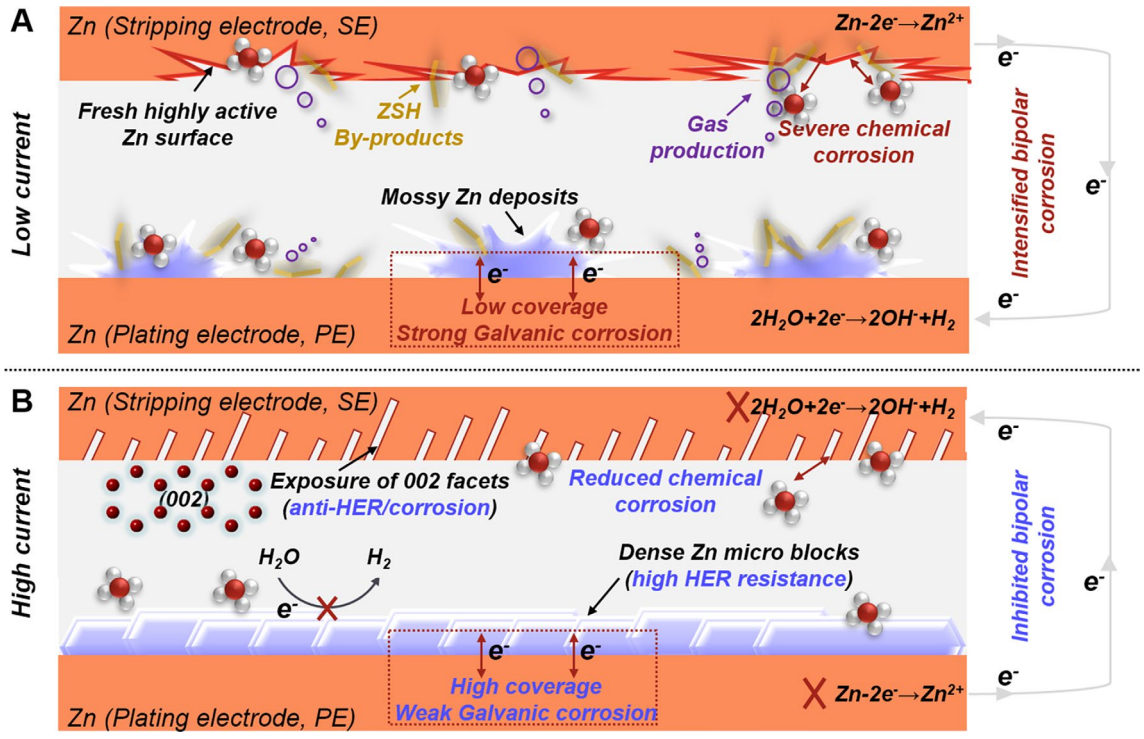

FIGURE 6 | Current-dependent Coupling electrochemical behaviors of Zn. (A, B) Zn plating, stripping, and corrosion behaviors at low-current density (A) and high-current density (B). High-current plating/stripping of Zn can enrich its highly stable (002) facets and form localized high-concentration electrolyte layers with solvated aggregates, which consequently suppresses hydrogen evolution reaction, dendrite formation, and surface corrosion.

high-current stripping process also contributed to uniform Zn dissolution, enhanced exposure of ultra-stable (002) facets, and the formation of transient high-concentration electrolyte environments containing solvated aggregates with reduced water reactivity, collectively mitigating the HER activity and surface corrosion of the SE. Benefiting from the favorable morphological, crystallographic, and solvation structural evolution during high-current plating/stripping, the cycling stability of Zn-MnO_2 full cells can be potentially improved by separately manipulating the Zn plating or stripping rates. Under circumstances where a low current discharging was required, the capacity retention of Zn-MnO_2 full cells can be significantly enhanced by 40% by increasing the charging current from 0.12 to 6 mA cm^{-2} (Figure S12).

2.6 | High-Current-Engineered Wide-Current Cyclable ZMA

Benefited from the exceptional anti-HER and corrosion-resistant capability of the high-current deposits, a wide-current cyclable ZMA was also developed via high-current pre-depositing a thin layer of dense Zn on top of the pristine foils (HC-Zn) (Figure S13). The preparation of the HC-Zn only required a pre-deposition of Zn on the pristine Zn foil at a high current of 50 mA cm^{-2} in low-cost aqueous zinc sulfate electrolyte, which was facile and easy to operate. Future optimizations in cell impedance, external circuits, electronic components, and electrochemical inputs can further decrease energy consumption via heat generation, promoting their commercial scaling up. Coupled with a DMSO-containing aqueous electrolyte, symmetric cells using HC-Zn anodes can sustain stable cycling and flat voltage evolution for over 4500 h at an extremely low-current density of 0.2 mA cm^{-2} in comparison to the pristine Zn anode with sudden voltage drop and quick short (Figure 7A). Compared with reported strategies, the as-developed HC-Zn enabled a record-breaking lifespan of 445 cycles and the highest accumulative capacity of 445 mAh cm^{-2} at 0.2 mA cm^{-2} (Figures 7B and S14). Note that pure organic systems were not fully compared here considering their poor compatibility for high-current cycling. Symmetric cells using the HC-Zn anode also demonstrated significantly

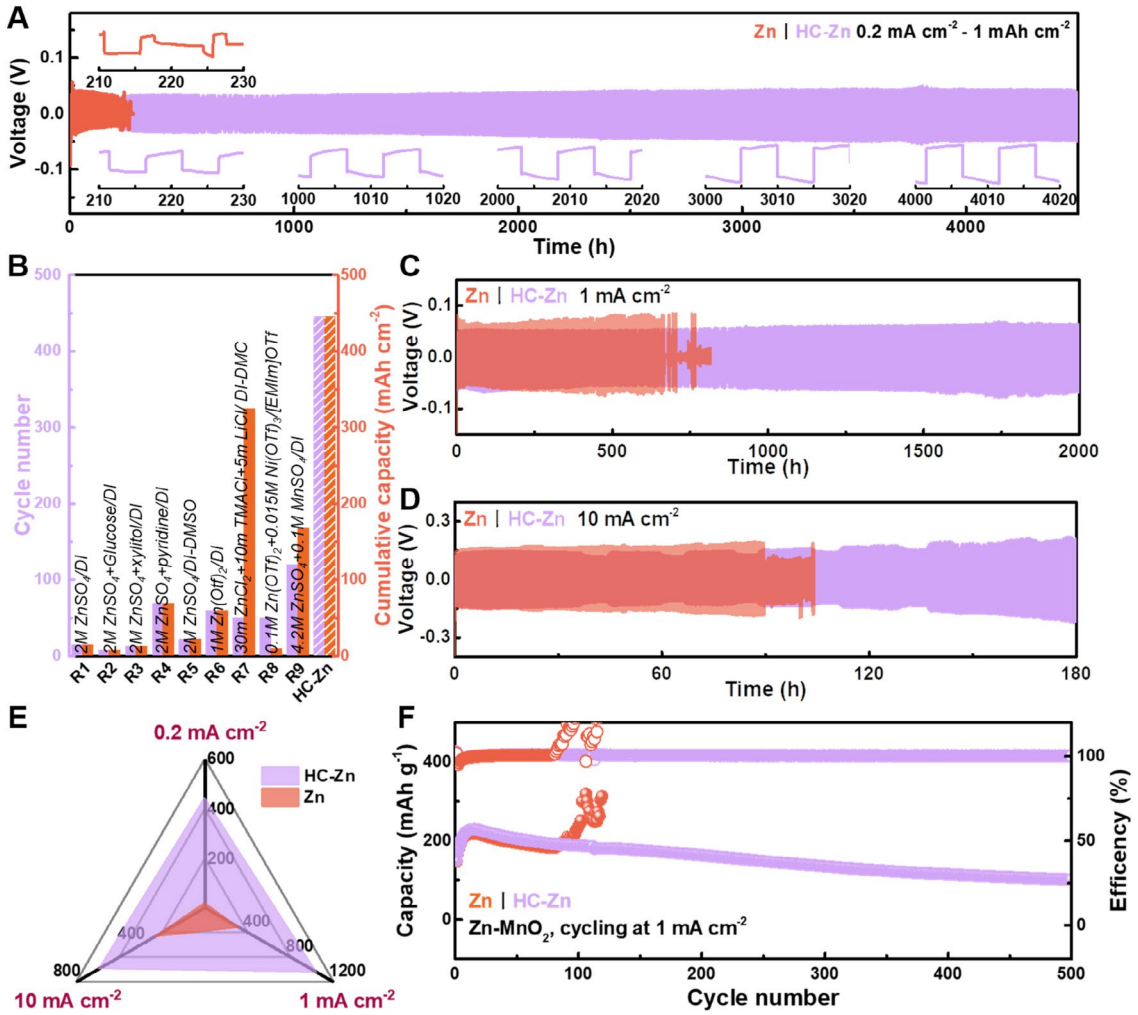

FIGURE 7 | High-current-engineered wide-current cyclable Zn (HC-Zn) anodes. (A) Voltage–time profiles of symmetric cells using HC-Zn and pristine Zn anodes upon cycling at extremely low current of 0.2 mA cm^{-2}. (B) Comparison of the cycling numbers and accumulative capacities between reported strategies and our work. (C, D) Voltage–time profiles of symmetric cells using HC-Zn and pristine Zn anodes upon cycling at 1 mA cm^{-2} (C) and 10 mA cm^{-2} (D). (E) Radar plot of the cycling numbers of the HC-Zn and pristine Zn anodes across a wide range of current densities. (F) Cycling performances of Zn-MnO_2 full cells at a low current of 1 mA cm^{-2} using the two anodes.

enhanced cycling stability at 1 mAh cm^{-2} and 10 mA cm^{-2} (Figure 7C,D). The radar plot in Figure 7E further implied the feasibility of the HC-Zn anodes to support stable cycling across a wide range of current densities. This strategy was also applicable to Li metal systems where an initial pre-deposition at a high current can also lead to enhanced reversibility of Li deposits and cycling stability [36].

The introduction of this pre-deposited Zn layer at high currents could lower the activation energy during charge transfer (Figure S15A). The plating of Zn on pristine Zn exhibited a significant voltage dip followed by a flat voltage plateau, leading to a large nucleation overpotential of 129 mV due to the thermodynamic mismatch toward the substrate. Comparatively, the nucleation overpotential of Zn on HC-Zn was near zero owing to the pre-implanted active Zn seeds (Figure S15B). Chronoamperometry (CA) characterization was further conducted to verify the mechanism of Zn plating behavior. The current evolutions under a constant potential can sensitively reflect the diffusion transitions. Therein, two-dimensional (2D) diffusion indicates the lateral diffusion of absorbed ions along the topmost surface to position the most energetically favorable sites for charge transfer, while three-dimensional (3D) diffusion implies the reduction of absorbed ions to Zn atoms for growth. Compared to the rampant 2D diffusion on pristine Zn foil, Zn plating on HC-Zn showed a largely restricted 2D diffusion (~5 s), reflecting a constant 3D diffusion after nucleation (Figure S15C). Zn-MnO_2 cells equipped with HC-Zn anodes also demonstrated significantly enhanced cyclability especially under a low current, showing a capacity retention of 67.3% after 500 cycles. In contrast, the Zn-MnO_2 cells using pristine Zn encountered huge fluctuations in CE and overcharging after cycling for 80 cycles.

3 | Conclusions

In summary, the current-dependent coupling behaviors among the plating, stripping, and corrosion of ZMA were uncovered across a wide current range from 0.2 to 10 mA cm^{-2}. A 50-fold decline in cycling lifespan was observed when the current density decreased from 10 to 0.2 mA cm^{-2} due to unfavorable evolution in morphological properties, crystallographic characteristics, and electrolyte solvation structures during low-current plating/stripping. Moreover, severe corrosion during Zn stripping instead of plating was discovered due to parasitic reactions between the newly exposed highly reactive fresh Zn surface and the aqueous electrolyte. This stripping-induced corrosion was significantly mitigated at 10 mA cm^{-2} owing to the 22-fold enhanced exposure of thermodynamically stable (002) facets. During resting, corrosion on the fresh Zn surface was even more severe compared to the stripping state. The faster release of Zn ions, especially during high-current stripping, reshaped the ion concentration and led to the formation of transient localized high-concentration electrolyte layers. Corresponding solvation structure also shifted from a contact-ion-pair dominant pattern to one dominated by solvated aggregates to effectively reduce the reactivity of the nearby electrolyte.

Guided by these fundamental insights, we have developed a highly stable ZMA, namely, HC-Zn. It possesses stable cycling across a wide current range from 0.2 to 10 mA cm^{-2}. In particular, HC-Zn exhibited a record-breaking lifespan of over 4500 h at 0.2 mA cm^{-2}. Smooth charging/discharging for over 500 cycles at a low current of 1 mA cm^{-2} was also achieved in Zn-MnO_2 full cells using HC-Zn. This work systematically analyzed the coupling interactions during Zn plating, stripping, and corrosion and offered fundamental insights for developing better ZMAs. It is anticipated that the implementation of multidimensional strategies comprising interfacial engineering, electrolyte optimization, and anode structure design will facilitate the realization of wide-current cyclability of AZMBs. From the perspective of the application of the AZMBs in grid-scale energy storage, it is also more imperative to improve the low-current cyclability than to constantly push the high-current limit of the ZMAs.

Author Contributions

Yanpeng Guo: writing – original draft preparation, data curation, validation. **Lutong Shan:** data curation, validation. **Yongqiang Yang:** formal analysis. **Junhua Zhou:** formal analysis. **Zijian Zheng:** supervision, funding acquisition, review and editing. Yanpeng Guo and Lutong Shan contributed equally to this work.

Acknowledgments

The authors acknowledge financial support from the RGC Postdoctoral Fellowship Scheme (PDFS2223_5S01), the RGC Research Impact Fund (R5019-22), and the Innovation and Technology Fund (GHP/047/20GD and PRP/055/21FX).

Conflicts of Interest

Zijian Zheng is Editor-in-Chief of EcoMat and co-author of this article. He was excluded from the peer-review process and all editorial decisions related to the acceptance and publication of this article. Peer review was handled independently by Associate Editor Qiang Zhang to minimize bias. The other authors declare no conflicts of interest.

References

1. S. W. D. Gourley, R. Brown, B. D. Adams, and D. Higgins, "Zinc-Ion Batteries for Stationary Energy Storage," *Joule* 7 (2023): 1415.

2. D. Lin and Y. Li, "Recent Advances of Aqueous Rechargeable Zinc-Iodine Batteries: Challenges, Solutions, and Prospects," *Advanced Materials* 34 (2022): 2108856.

3. S. Liu, R. Zhang, C. Wang, et al., "Zinc Ion Batteries: Bridging the Gap From Academia to Industry for Grid-Scale Energy Storage," *Angewandte Chemie, International Edition* 63 (2024): e202400045.

4. C.-X. Bi, L.-P. Hou, Z. Li, et al., "Protecting Lithium Metal Anodes in Lithium–Sulfur Batteries: A Review," *Advanced Energy Materials* 4 (2023): 10.

5. J. H. Song, K. Xu, N. Liu, D. Reed, and X. L. Li, "Crossroads in the Renaissance of Rechargeable Aqueous Zinc Batteries," *Materials Today* 45 (2021): 191.

6. C. Li, S. Jin, L. A. Archer, and L. F. Nazar, "Toward Practical Aqueous Zinc-Ion Batteries for Electrochemical Energy Storage," *Joule* 6 (2022): 1733.

7. W. Chen, Y. Wang, F. Wang, et al., "Zinc Chemistries of Hybrid Electrolytes in Zinc Metal Batteries: From Solvent Structure to Interfaces," *Advanced Materials* 36 (2024): 2411802.

8. Z. Yi, G. Chen, F. Hou, L. Wang, and J. Liang, "Strategies for the Stabilization of Zn Metal Anodes for Zn-Ion Batteries," *Advanced Energy Materials* 11 (2021): 2003065.

9. H. Yan, S. Li, J. Zhong, and B. Li, "An Electrochemical Perspective of Aqueous Zinc Metal Anode," *Nano-Micro Letters* 16 (2023): 15.

10. K. Zhou, X. Yu, X. Dong, Z. Guo, and Y. Wang, "Strategies and Prospects for Engineering a Stable Zn Metal Battery: Cathode, Anode, and Electrolyte Perspectives," *Accounts of Chemical Research* 58, no. 4 (2025): 599–611, https://doi.org/10.1021/acs.accounts.4c00776.

11. P. Ruan, S. Liang, B. Lu, H. J. Fan, and J. Zhou, "Design Strategies for High-Energy-Density Aqueous Zinc Batteries," *Angewandte Chemie, International Edition* 61 (2022): 2200598.

12. G. Zampardi and F. La Mantia, "Open Challenges and Good Experimental Practices in the Research Field of Aqueous Zn-Ion Batteries," *Nature Communications* 13 (2022): 687.

13. H. Wang, R. Tan, Z. Yang, Y. Feng, X. Duan, and J. Ma, "Stabilization Perspective on Metal Anodes for Aqueous Batteries," *Advanced Energy Materials* 11 (2021): 2000962.

14. M. Wu, Y. Zhang, L. Xu, et al., "A Sustainable Chitosan-Zinc Electrolyte for High-Rate Zinc-Metal Batteries," *Matter* 5 (2022): 3402.

15. J. Jiang, Y. Chen, Y. Li, et al., "Regulating Zn^{2+} Solvation Structure in Eutectic Electrolytes for Rechargeable Zinc Batteries," *Matter* 8, no. 2 (2025): 101917, https://doi.org/10.1016/j.matt.2024.11.011.

16. J.-L. Yang, P. Yang, T. Xiao, and H. J. Fan, "Designing Single-Ion Conductive Electrolytes for Aqueous Zinc Batteries," *Matter* 7 (2024): 1928.

17. H. Peng, Y. Fang, J. Wang, et al., "Constructing Fast-Ion-Conductive Disordered Interphase for High-Performance Zinc-Ion and Zinc-Iodine Batteries," *Matter* 5 (2022): 4363.

18. X. Guo, H. Hong, Q. Li, et al., "Dual Robust Electrode-Electrolyte Interfaces Enabled by Fluorinated Electrolyte for High-Performance Zinc Metal Batteries," *Matter* 7 (2024): 4014.

19. L. Sun, Y. Wang, K. Zhang, et al., "Stable Zinc Metal Anodes Achieved by Dynamic Counteracting Tip Effect and Interfacial Ion Redistribution," *Journal of Energy Chemistry* 99 (2024): 172.

20. Y. Ahn, J. Baek, S. Kim, et al., "Unveiled Mechanism of Prolonged Stability of Zn Anode Coated With Two-Dimensional Nanomaterial Protective Layers Toward High-Performance Aqueous Zn Ion Batteries," *EcoMat* 6 (2024): e12482.

21. J. D. Wang, B. Zhang, Z. Cai, et al., "Stable Interphase Chemistry of Textured Zn Anode for Rechargeable Aqueous Batteries," *Science Bulletin* 67 (2022): 716.

22. Y. Li, X. Ma, X. Zhang, et al., "High Zn(002)-Preferential Orientation Enabled by a Proton Additive for Dendrite-Free Zinc Anodes," *Energy & Environmental Science* 17 (2024): 9205.

23. Y. H. Zou, X. Z. Yang, L. Shen, et al., "Emerging Strategies for Steering Orientational Deposition Toward High-Performance Zn Metal Anodes," *Energy & Environmental Science* 15 (2022): 5017.

24. Z. Yang, C. Hu, Q. Zhang, et al., "Bulk-Phase Reconstruction Enables Robust Zinc Metal Anodes for Aqueous Zinc-Ion Batteries," *Angewandte Chemie, International Edition* 62 (2023): e202308017.

25. R. Guo, X. Liu, K. Ni, et al., "Non-Destructive Stripping Electrochemistry Enables Long-Life Zinc Metal Batteries," *Energy & Environmental Science* 18, no. 5 (2025): 2353–2364, https://doi.org/10.1039/d4ee05044d.

26. B. Liu, Z. Xu, C. Wei, et al., "Re-Understanding and Mitigating Hydrogen Release Chemistry Toward Reversible Aqueous Zinc Metal Batteries," *eScience* (2024): 100330, https://doi.org/10.1016/j.esci.2024.100330.

27. Z. Zhao, Y. He, W. Yu, W. Shang, Y. Ma, and P. Tan, "Revealing the Missing Puzzle Piece of Concentration in Regulating Zn Electrodeposition," *Proceedings of the National Academy of Sciences of the United States of America* 120 (2023): e2307847120.

28. M. Xi, Z. Liu, W. Wang, et al., "Shear-Flow Induced Alignment of Graphene Enables the Closest Packing Crystallography of the (002) Textured Zinc Metal Anode With High Reversibility," *Energy & Environmental Science* 17 (2024): 3168.

29. M. Zhou, S. Guo, J. Li, et al., "Surface-Preferred Crystal Plane for a Stable and Reversible Zinc Anode," *Advanced Materials* 33 (2021): 2100187.

30. X. Yu, M. Chen, Z. Li, et al., "Unlocking Dynamic Solvation Chemistry and Hydrogen Evolution Mechanism in Aqueous Zinc Batteries," *Journal of the American Chemical Society* 146 (2024): 17103.

31. J. M. Zheng, P. F. Yan, D. H. Mei, et al., "Highly Stable Operation of Lithium Metal Batteries Enabled by the Formation of a Transient High-Concentration Electrolyte Layer," *Advanced Energy Materials* 6 (2016): 1502151.

32. A. Kolesnikov, M. Kolek, J. F. Dohmann, et al., "Galvanic Corrosion of Lithium-Powder-Based Electrodes," *Advanced Energy Materials* 10 (2020): 2000017.

33. D. T. Boyle, W. Huang, H. Wang, et al., "Corrosion of Lithium Metal Anodes During Calendar Ageing and Its Microscopic Origins," *Nature Energy* 6 (2021): 487.

34. D. Lin, Y. Liu, Y. Li, et al., "Fast Galvanic Lithium Corrosion Involving a Kirkendall-Type Mechanism," *Nature Chemistry* 11 (2019): 382.

35. Z. Cai, J. Wang, and Y. Sun, "Anode Corrosion in Aqueous Zn Metal Batteries," *eScience* 3 (2023): 100093.

36. Y. P. Guo, X. Q. Wei, C. Zeng, et al., "In Situ Analysis of Li Plating and Stripping Behaviors Under Dynamic Current Conditions for Realistic Application Scenarios," *Advancement of Science* 12 (2025): 2414396.

Supporting Information

Additional supporting information can be found online in the Supporting Information section.